Magnetic vortex dynamics in thickness-modulated $Ni_{80}Fe_{20}$ disks

G. Shimon,[1,2] A. O. Adeyeye,[1,2,*] and C. A. Ross[2,3,†]

[1]*Department of Electrical and Computer Engineering, 4 Engineering Drive 3, National University of Singapore, Singapore 117576, Singapore*

[2]*Singapore-MIT Alliance, 4 Engineering Drive 3, Singapore 117576, Singapore*

[3]*Department of Materials Science and Engineering, Massachusetts Institute of Technology, Cambridge, Massachusetts 02139, USA*

(Received 15 April 2013; revised manuscript received 28 May 2013; published 21 June 2013)

The magnetic vortex dynamics in thickness-modulated $Ni_{80}Fe_{20}$ disks in the form of a $Ni_{80}Fe_{20}$ lens on top of a $Ni_{80}Fe_{20}$ disk are investigated. The vortex core location can be systematically controlled via the geometry, and the propagation and annihilation can be detected using ferromagnetic resonance measurements. The thickness modulation provides an additional shape anisotropy, which defines the vortex chirality in the disk depending on the magnetization reversal history and the magnetic interactions between the disk and the lens. The vortex propagation and annihilation in each layer were identified by their resonance modes.

DOI: 10.1103/PhysRevB.87.214422 PACS number(s): 75.75.−c, 75.78.−n, 76.50.+g, 62.23.Eg

I. INTRODUCTION

The dynamic behavior of patterned thin film magnetic elements in the gigahertz regime is of interest for high-frequency memory elements,[1,2] logic devices,[3–5] and magnonic filters.[6,7] There are many reports on the dynamic behavior of patterned magnetic elements of various shapes, including squares,[8,9] rectangles,[10,11] triangles,[12] stripes,[13,14] wires,[15,16] ellipses,[17,18] circular disks,[19–21] and rings.[22–24] Among these examples, circular disks have attracted the most interest due to their simplicity and their potential applications. Since the pioneering papers by Shinjo *et al.*[25] and Cowburn *et al.*,[26] it is well known that magnetic disks will form a vortex magnetization state beyond a certain critical radius (R_C) for a given thickness as a result of competition between exchange and magnetostatic energies. The quasistatic reversal of magnetic disks has been well investigated.[26–30] Unlike the saturated or single-domain state, a vortex state has an in-plane curling magnetization and a small region of vortex core whose magnetization points out of the plane. For this reason, a vortex state is commonly identified by two parameters: core polarity ($p = +1$ or -1 for a vortex core oriented up or down, respectively) and chirality ($c = +1$ or -1 for a vortex curling clockwise [CW] or counterclockwise [CCW], respectively). There are also several analytical approaches to describe vortex nucleation and annihilation. For example, using the Usov and Peschany[31] formulation for the curling magnetization of a vortex ground state, Guslienko and Metlov[32] developed a "rigid vortex" model for a vortex state under an applied field and used the model to estimate the nucleation and annihilation fields (H_N and H_A, respectively) based on energy minimization. This model can also be modified to account for interdisk magnetostatic coupling during vortex reversal.[33]

The excitations of vortex states in magnetic disks are broadly divided into two categories: gyrotropic and magnetostatic modes. The gyrotropic mode is characterized by an oscillatory mode (gyration) of the vortex core around its equilibrium position when it is excited by magnetic fields[21,34,35] or spin-polarized current.[1,36–39] Generally, the gyrotropic frequency is in the range of hundreds of megahertz. In contrast, the magnetostatic mode has a relatively high excitation frequency of several gigahertz. In circular or cylindrical disks, this mode is manifested in the form of radial and azimuthal modes.[17,19] Both gyrotropic and magnetostatic modes are highly dependent on the sample geometry and materials.

While numerous reports show the manipulation of vortex core polarity in magnetic disks,[1,35,39–44] there have been fewer reports of the control of vortex chirality.[45–47] This has been done by introducing configurational anisotropy,[45] by coupling between disks,[47] or by fabricating a D-shaped disk.[48,49] These reports have focused primarily on investigating the static behavior of the disks. In this report, we present dynamic studies of the vortex state in thickness-modulated $Ni_{80}Fe_{20}$ (permalloy or NiFe) disks in the form of a $Ni_{80}Fe_{20}$ lens shape on top of a $Ni_{80}Fe_{20}$ disk [Fig. 1(b)]. Using an angle-deposition technique to produce the thickness modulation, we introduce an alternative approach to achieve vortex chirality control in isolated disks. We show that the onset of vortex propagation can be determined using ferromagnetic resonance (FMR) by detecting a specific resonance mode. The thickness modulation introduces an additional shape anisotropy, which controls the vortex chirality during magnetization reversal. The thickness modulation also modified the magnetostatics of the disk such that the vortex core location and its propagation direction can be controlled. Moreover, due to the lateral confinement of the vortex core within the NiFe lens, we can provide direct experimental evidence of well-controlled vortex chirality using magnetic force microscopy (MFM).

This paper also describes the vortex dynamics when the lens-shaped region is exchange decoupled from the disk by a Cu spacer. Interlayer coupling effects on a high-frequency response are important in the design of tunable magnetic band stop filters in mobile applications[50] utilizing continuous or patterned films. However, most papers have focused on the effect of dipolar coupling in comparison to a single-layer system,[50–53] and there is little work that systematically investigates a range of spacer thicknesses. Here, the onset of vortex propagation in each magnetostatically coupled layer was detected using FMR, and the effects of the antiparallel alignment between the magnetostatically coupled NiFe lens and the disk layers on the static and dynamic behavior of the disk were demonstrated.

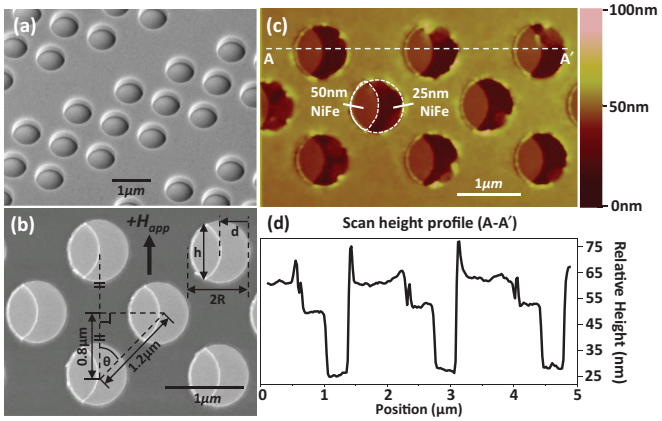

FIG. 1. (Color online) SEMs of (a) three-dimensional resist profiles for the disks and (b) thickness-modulated NiFe disks. (c) AFM image of thickness-modulated NiFe disks embedded in the BARC layer, and (d) the corresponding scan height profile taken along line A-A′, as indicated in panel (c).

II. EXPERIMENTAL METHODS

A resist film on a silicon substrate was exposed and developed to form an array of circular holes, as shown in Fig. 1(a), using deep ultraviolet lithography at a 248-nm exposure wavelength. Details of the resist pattern fabrication process were described previously.[54] An array of thickness-modulated disks was made by a series of thin film depositions at different angles onto the resist patterns. In the first step, a 25-nm-thick NiFe layer was deposited at normal incidence. Subsequently, a shadow deposition step was performed at 45° from normal incidence to achieve partial coverage of the patterned holes. In this step, the top NiFe layer (25 nm) formed lens-shaped structures on the disks due to shadowing from the resist profile. In some samples, a Cu spacer layer (t_{Cu} nm) was deposited to separate the two NiFe layers. The angle deposition technique has been described elsewhere.[55] The NiFe layers were deposited using electron beam evaporation at a rate of 0.2 Å/s with a base pressure of 4×10^{-8} Torr. The Cu spacer layer was deposited using magnetron sputter deposition at 3-mTorr working pressure and 50-W power, which gave a deposition rate of 0.27 Å/s in the same chamber. Photoresist removal was done by soaking the patterned film in OK73 resist thinner. Successful liftoff was determined visually and confirmed using scanning electron microscopy. Figure 1(b) shows a scanning electron micrograph (SEM) of the resulting disks of a 800-nm diameter with a thickness modulation, i.e., 25-nm NiFe circular disks with an additional 25-nm layer of lens-shaped NiFe on top. The center-to-center distance between the features was 1.2 μm along the diagonal direction or 1.6 μm along the horizontal direction, which reduced magnetostatic interactions within the array.

To estimate magnetostatic interactions between the disks, the interaction field was approximated as a dipolar field $H_{dip}(r)$ from a magnetic moment m by approximating the disk as a current loop:[56]

$$H_{dip}(r) = 2\left(\frac{m}{r^3}\right)\cos\theta \qquad (1)$$

where m is the total magnetic moment of the thickness-modulated disk in electromagnetic units, r is the distance away from the center of the dipole, and θ is the angle between the measurement direction and the direction of magnetization, as indicated in Fig. 1(b). The bottom NiFe disk with radius $R = 400$ nm and thickness $t_d = 25$ nm has volume $V_d = 1.26 \times 10^{-14}$ cm^3. The NiFe lens is approximated by two intersecting circles with the area $A_l = \pi R^2 - 2R^2 \tan^{-1}(\frac{d}{h}) - \frac{1}{2}dh$, where $h = \sqrt{4R^2 - d^2}$, with d as the offset between the two intersecting circles and h as the length of the lens, as indicated in Fig. 1(b). For $R = 400$ nm, $t_l = 25$ nm, and $h = 700$ nm from the SEM, the lens volume $V_l = 0.51 \times 10^{-14}$ cm^3, which is ~41% of V_d. Assuming the disk is in the saturated state with $M_s = 860$ emu cm^{-3} gives $H_{dip}(r) = 12$ Oe for neighboring disks along the diagonal of the array, which is small compared with the switching fields described below.

Figure 1(c) shows the atomic force microscope (AFM) image and Fig. 1(d) shows the height profile of the thickness-modulated disks along line A-A′. The disks are surrounded by a 60-nm-thick bottom antireflection coating (BARC) layer, but a clear thickness modulation in the NiFe is evident. The magnetic states were imaged using MFM with a CoCr-coated tip at a scan height of 100 nm to minimize the interactions between the disks and the tip. The collective magnetic switching behavior of disk arrays was characterized by focused magneto-optical Kerr effect (MOKE) with a spot size of ~50 μm in longitudinal geometry, which measures ~1100–1200 disks simultaneously.

To excite and detect FMR, a ground-signal-ground (G-S-G) type of coplanar waveguide (CPW) was fabricated on top of it. To fabricate the CPWs, standard photolithography and deposition of Al_2O_3(50 nm)/Ti(5 nm)/Au(200 nm) were used. The FMR response of the nanostructures was measured using a microwave vector network analyzer (VNA). The VNA was connected to the CPWs using G-S-G-type microwave coplanar probes. The FMR response was measured at room temperature by sweeping the frequency for fixed applied field (H_{app}) in the 1- to 20-GHz range. This process was repeated for a series of H_{app} values from a negative saturation field of −1400 Oe to a positive saturation field of 1400 Oe. A reference signal was measured prior to the actual sample measurement to subtract the background noise from the measurement.

Micromagnetic simulations were performed using the LLG Micromagnetics Simulator.[57] The saturation magnetization was taken as $M_{s,NiFe} = 860$ emu cm^{-3}, the exchange constant was $A_{NiFe} = 13 \times 10^7$ erg cm^{-1}, and the magnetocrystalline anisotropy was $K_{1,NiFe} = 0$. A unit cell size with a $10 \times 10 \times 5$-nm thickness was used in the simulations. A simulation using a smaller cell, $5 \times 5 \times 5$ nm, gave similar results. The masks used in the simulations were extracted from SEMs of the fabricated structures. For quasistatic simulation, a damping coefficient of $\alpha = 0.5$ was chosen to obtain a rapid convergence. To simulate the FMR response and quantify the spatial characteristics of different resonance modes, time-dependent micromagnetic simulations were performed using a gyromagnetic ratio $\frac{\gamma}{2\pi} = 2.8$ GHz/kOe and $\alpha = 0.008$. The dynamic simulation results were analyzed in the frequency domain by performing fast Fourier transform processing.

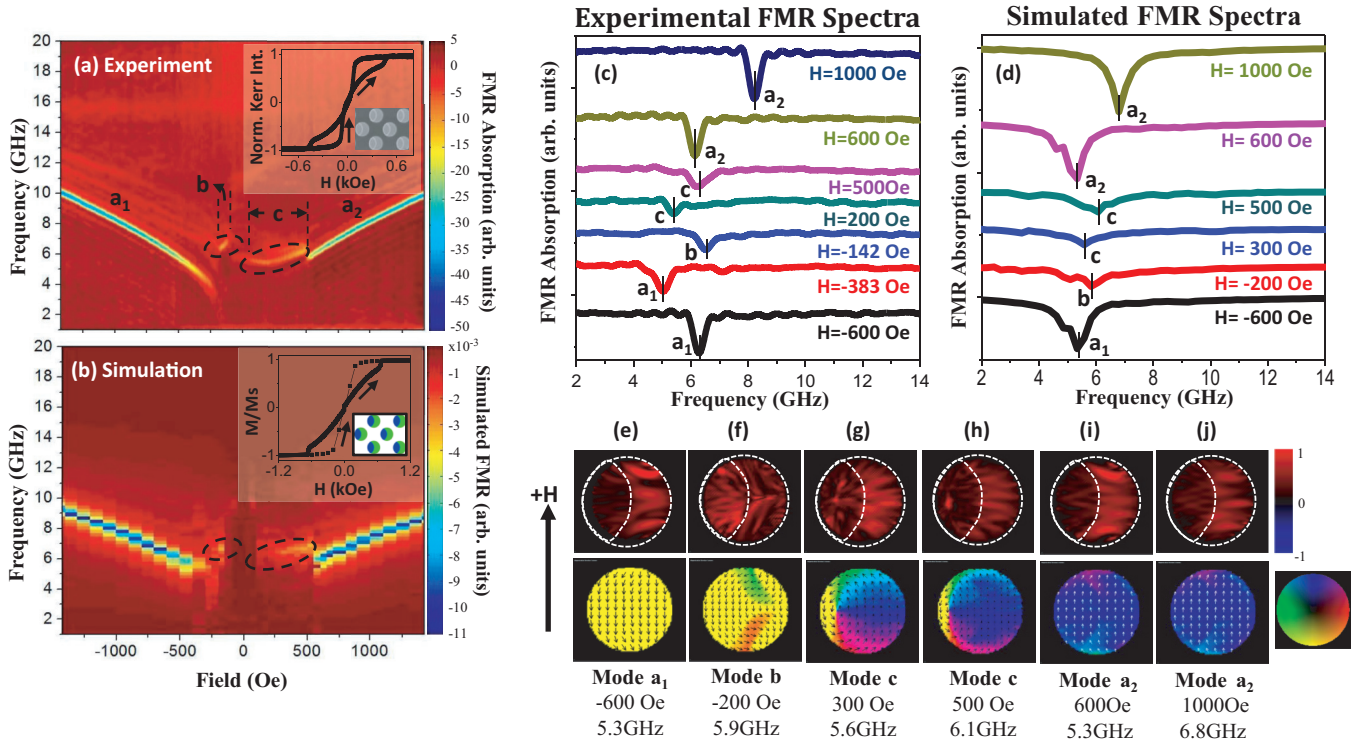

FIG. 2. (Color online) (a) Experimental and (b) simulated FMR absorption spectra for thickness-modulated disks ($t_{Cu} = 0$ nm). Color scale bars represent relative FMR absorption intensity. (c) Experimental and (d) simulated FMR absorption spectra for selected H_{app}. (e)–(j) Simulated mode profiles (upper panels) and the corresponding static magnetic configurations (lower panels) at various H_{app}. Color scale bar next to (j) (upper panel) represents normalized FMR absorption for (e)–(j). Color wheel next to (j) (lower panel) represents the component of in-plane magnetization in the disks. Insets in (a) and (b) are the experimental MOKE loop and simulated hysteresis loop, respectively.

III. RESULTS AND DISCUSSION

A. Vortex dynamic response

Figure 2(a) shows the FMR absorption spectra measured for thickness-modulated disks. The relative FMR absorption peaks are plotted as a function of applied field H_{app} for the frequency range of 1–20 GHz. To understand the origin of FMR spectra, a series of dynamic simulations was performed to obtain simulated FMR spectra in Fig. 2(b). There was a remarkably good agreement between experimental and simulated FMR spectra in terms of the peaks observed. However, the resonance frequency (f_{res}) values are lower in the simulation than in the experiment, which could be related to the 0 K temperature assumptions in the simulation.

Before discussing the dynamic behavior of the disk, it is important to understand its static reversal mechanism. The static reversal behavior was investigated by measuring the MOKE loop of the sample and calculating the corresponding hysteresis loop from micromagnetics, which are shown as insets in Figs. 2(a) and 2(b), respectively. The H_{app} direction for all measurements is along the y direction, parallel to the axis of the lens, as indicated next to Fig. 2(e). The experimental MOKE loop agrees well with the simulation in terms of overall shape, though the switching fields are about twice as large in the simulation, again attributed to thermal effects not included in the simulation. The MOKE loop showed two switching steps, which are assigned to the vortex nucleation field $H_N = -68$ Oe and vortex annihilation field $H_A = 457$ Oe. This reversal via vortex nucleation and annihilation is commonly observed in circular disks with $R > R_C$. Based on the thickness range of 25–50 nm for our thickness-modulated disk, we estimated $R_C < 100$ nm.[26] Therefore, we should expect the disks to reverse via vortex formation. The switching field values from the MOKE loop were determined by taking the first derivative of the Kerr intensity plot in the ascending sweep direction to get the peak positions. The two-step switching is confirmed by the simulation, which gives $H_N = 0$ Oe and $H_A = 600$ Oe. Figure 2(e) shows the magnetic configurations at selected H_{app} from the simulation. Since the bottom NiFe disk and top NiFe lens layers are exchange coupled, the moments in each layer where they overlap had similar configurations. By reducing H_{app} from negative saturation, the magnetic moments in the disks relaxed to follow the circumference of the disks due to shape anisotropy. At -200 Oe, the bottom NiFe disk formed a transverse wall (TW), while the top NiFe lens was in a "C" state. The formation of the TW configuration was followed by vortex nucleation at 0 Oe. As expected, the vortex was nucleated in the thicker region (50 nm thick) of the disks [Fig. 2(g), lower panel].[26] As the field increased, the vortex started to move toward the left (compare configurations at 300 and 500 Oe) and annihilated on the left side of the disk at 600 Oe. Further analysis of the static behavior is described in Sec. III B.

Three distinct resonance modes in Fig. 2(a) were observed as H_{app} was swept from -1400 to 1400 Oe. The first mode

occurred as the field was reduced from negative saturation, with a decrease in f_{res} as the field was reduced. In Fig. 2(c), the absorption spectrum for $H_{app} = -600$ Oe is shown with the main peak (labeled a_1) at 6.28 GHz, which decreased to 5.04 GHz for $H_{app} = -383$ Oe. In Fig. 2(d), the simulated FMR shows the peak a_1 at 5.3 GHz for $H = -600$ Oe. The mode profile of a_1 in Fig. 2(e) reveals that the absorption originated in the 25-nm-thick region of the disk, i.e., the part not covered by the lens. The decrease in f_{res} is related to the modification of effective field along the y direction. We recall the Kittel formulation[58]

$$f = \frac{\gamma}{2\pi}\sqrt{(H_y + (N_z - N_y)4\pi M_y)\,(H_y + (N_x - N_y)4\pi M_y)} \tag{2}$$

where N_x, N_y, and N_z are the demagnetizing factors for x, y, and thickness (z) directions respectively; γ is the gyromagnetic ratio of the materials; and $4\pi M_y$ is the magnetization of the sample along H_{app} i.e., along the y direction. The mode a_1 shifted to lower f_{res} due to reduction in the effective field in the y direction, H_y; i.e., f_{res} reduced from 10 to 3.46 GHz (62% decrease) as H_{app} was swept from -1400 to around -210 Oe.

The a_1 peak disappeared at $H_{app} = -210$ Oe, while another absorption peak, labeled b, appeared with $\Delta f_{a1\to b} = 2.86$ GHz or $f_{res,b}$ of $\sim$1.8 times that of $f_{res,a1}$. In Fig. 2(c), the extracted FMR spectrum for $H_{app} = -142$ Oe shows mode b at 6.52 GHz. The simulated spectrum at -200 Oe [Fig. 2(d)] shows mode b at 5.9 GHz. As discussed above, at -200 Oe, the bottom NiFe disk had a TW configuration, while the top NiFe lens was in "C" state. Looking closely at Fig. 2(f), the mode profile b reveals that much of the absorption comes from the 50-nm-thick lens-shaped region of the disk. To investigate the abrupt increase in f_{res}, we must analyze the change in H_y as mode b appears. two competing factors in determining H_y in this case are H_d and H_{app}, according to the effective field expression $H_y = H_{app} - H_d$ in the Kittel formulation ($-H_d$ shows the demagnetizing field has a direction opposite to that of H_{app}). In the disk at -200 Oe, the formation of the "C" state significantly reduces the demagnetizing field H_d from this region, which contributes to an increase in H_y. At the same time, reduction of H_{app} reduces H_y. The condition for the abrupt increase in f_{res} implies that H_y must have increased when mode a_1 transitioned to mode b, i.e., the decrease in H_d was the dominant contribution.

The mode b frequency increased in the experiment from 6.32 to 7.0 GHz as the field was reduced from -170 to -92 Oe; i.e., a negative dispersion ($df_{res}/dH < 0$) was observed. This can be attributed to the overall increase in H_y as the curvature of the "C" state becomes larger with decreasing field, causing a further reduction in H_d. It is also possible that a reverse domain opposite to the H_{app} may have formed in the 50-nm-thick region, producing H_d parallel to H_{app}, although the simulation did not show this or the increase in f_{res} with decreasing field. Mode b finally disappeared when the vortex was nucleated.

Another resonance mode, labeled c, appeared at $\sim$50 Oe. Figures 2(g) and 2(h) suggest that mode c is localized in the 25-nm-thick region of the disks and from the vortex core, and the simulation mode profiles suggest that mode c is excited during vortex core propagation in the disk. Mode c is the magnetostatic mode of vortex propagation. The small circular absorption region in the NiFe lens follows the vortex core location. This indicates that we can use FMR to trace the onset of vortex propagation prior to vortex annihilation, which is difficult to obtain from the experimental hysteresis loop. The f_{res} of mode c increased with increasing H_{app} in both the experiment ($\delta f_{res} = 1.05$ GHz from 200 to 525 Oe) and the simulation ($\delta f_{res} = 0.51$ GHz from 250 to 500 Oe), attributed to the increase in H_y as H_{app} increases, and the enlargement of the region of magnetization aligned with H_{app} as the vortex core moves toward the left.

When the vortex annihilated, mode c disappeared while mode a_2 appeared. Mode a_2 is analogous to mode a_1 discussed earlier, and its f_{res} dropped compared to mode c in both the experiment ($\delta f_{c\to a2} = 1.11$ GHz) and the simulation ($\delta f_{c\to a2} = 0.91$ GHz). As the vortex annihilates, there is an increase in the fraction of the disk magnetized parallel to H_{app}, which lowered H_y and f_{res}.

B. Control of vortex chirality and propagation

Having demonstrated the dynamic detection of the vortex state in the thickness-modulated disks by FMR, we now discuss the vortex chirality and propagation control, which can be achieved in this structure. The disks exhibited a specific chirality preference depending on the direction of the field reversal. When H_{app} was swept from negative to positive saturation, a CCW chirality was obtained for all disks [Figs. 2(g) and 2(h), lower panel]. The vortex chirality became CW when the H_{app} sweep direction was reversed. This is attributed to a lack of symmetry in the lens-shaped layers, which had a longer arc length on the left side than on the right side. The asymmetry in the lens enhanced the shape anisotropy of the disk and caused the magnetic moments to curve along the longer arc of the lens [Fig. 2(f), lower panel], defining the vortex chirality of the disk. The experimental MFM evidence of chirality control is presented in Fig. 3. The MFM images were taken at remanence after each minor loop cycling at selected H_{rev} (i.e., field cycling is -3 kOe $\to$ H_{rev} $\to$ 0 Oe). At $H_{rev} = 0$ Oe, disks with thickness modulation showed uniform chirality [Fig. 3(a)] i.e., CCW, which was also maintained at

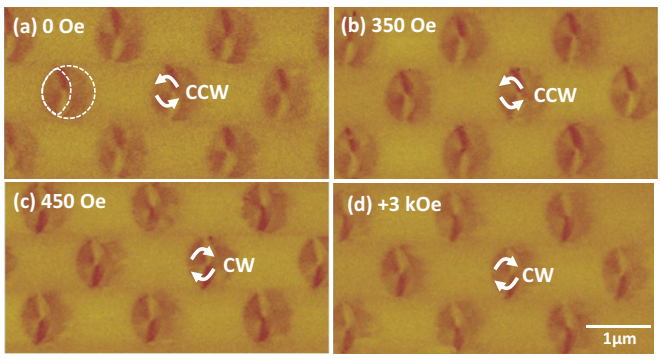

FIG. 3. (Color online) MFM images of thickness-modulated disks taken at remanence after applying a negative saturating field of -3 kOe and then cycling to various reversal fields: (a) 0 Oe, (b) 350 Oe, (c) 450 Oe, and (d) +3 kOe.

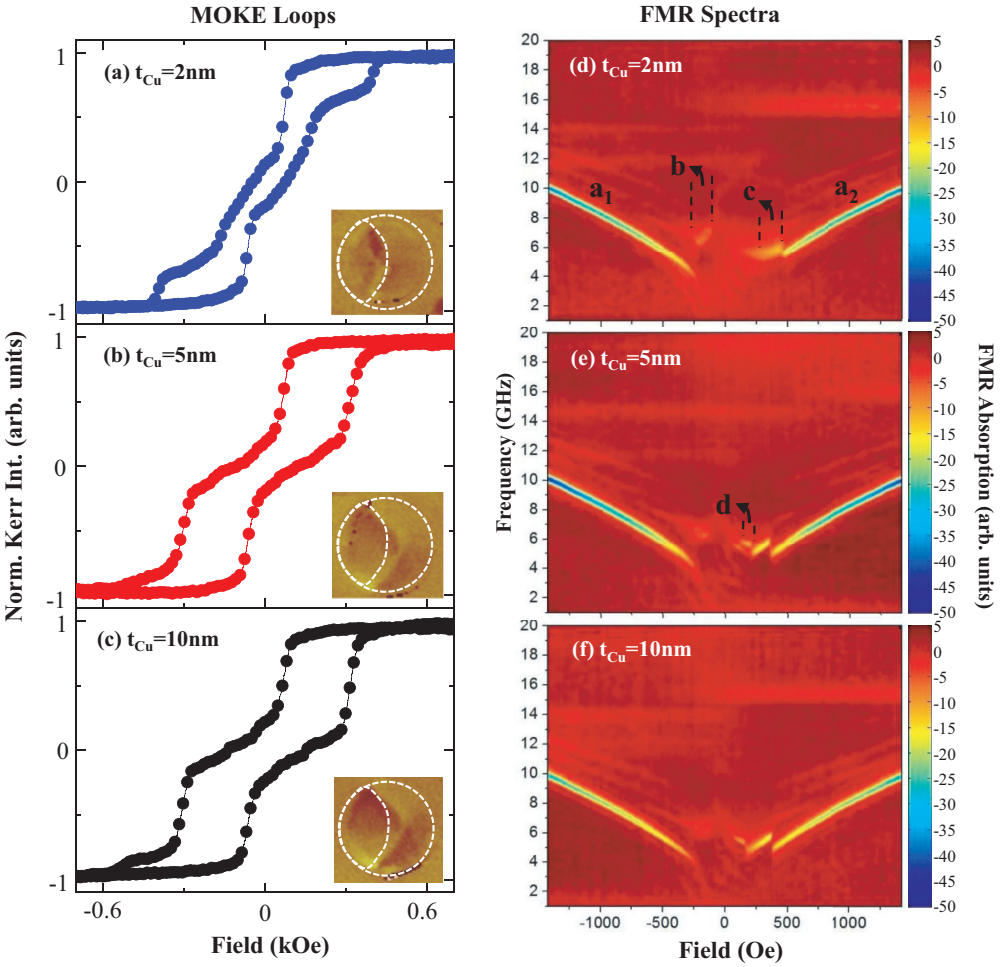

FIG. 4. (Color online) Experimental MOKE loops for thickness-modulated disks with (a) $t_{Cu} = 2$ nm, (b) $t_{Cu} = 5$ nm, and (c) $t_{Cu} = 10$ nm. Insets are the corresponding MFM images taken at remanence after applying a negative saturating field of -3 kOe. Experimental FMR absorption spectra for thickness-modulated disks with (d) $t_{Cu} = 2$ nm, (e) $t_{Cu} = 5$ nm, and (f) $t_{Cu} = 10$ nm. Color scale bars represent relative FMR absorption intensity.

$H_{rev} = 350$ Oe [Fig. 3(b)] prior to vortex annihilation. For $H_{rev} = 450$ Oe [Fig. 3(c)], which is $\sim H_A$, the vortex chirality at remanence reversed to become CW. Similarly, CW chirality was obtained when a large reverse field $H_{rev} = 3$ kOe was applied and then removed [Fig. 3(d)], so the vortex chirality can be controlled by field cycling.

The vortex consistently moved toward and annihilated on the left (thicker) side of the disk regardless of its chirality. This occurred because the vortex is energetically more favorable in the thicker part of the disk.[26] This argument is supported by means of calculating the volume-normalized total energy E_{tot} of a vortex in 50-nm-thick NiFe disk ($E_{tot} = 3.64 \times 10^3$ Jm^{-3}), which is about quarter that of a 25-nm NiFe disk ($E_{tot} = 1.34 \times 10^4$ Jm^{-3}).

C. Effect of interlayer magnetostatic interaction

To investigate the behavior of thickness-modulated disks in which the two layers of the NiFe are exchange decoupled, a Cu spacer layer with varying thickness (t_{Cu}) was formed between the NiFe disk and lens. The MOKE loop measurements for $t_{Cu} = 2$, 5, and 10 nm are plotted in Figs. 4(a)–4(c). For each t_{Cu} case, the MFM contrast taken at remanence is shown as an inset. The MOKE loop for $t_{Cu} = 2$ nm showed a significant shift in Kerr intensity (away from zero) in the range of ± 200 Oe compared to the case of $t_{Cu} = 0$ nm. In this structure, the exchange coupling between the two layers was reduced if not eliminated, allowing different reversal paths for the two layers.[26,28] The MFM contrast [inset in Fig. 4(a)] still clearly showed the presence of a CCW vortex at remanence, which was centered in the top NiFe lens, similar to the case of $t_{Cu} = 0$ nm. In Figs. 4(b) and 4(c), MOKE loops for both $t_{Cu} = 5$ and 10 nm showed a clear departure from the case of $t_{Cu} = 0$ nm. The thick Cu spacer layer enabled the disk and lens to reverse separately, and the vortex was centered in the disk, as shown in the insets of Figs. 4(b) and 4(c). Two switching fields were identified as H_N and H_A, similar to the case of $t_{Cu} = 0$ nm.

The FMR responses for varying t_{Cu} are given in Figs. 4(d)–4(f). Modes a_1 and a_2 were present in all cases with little or no change in the f_{res} value at high fields. Mode b became weaker while mode c became stronger with increasing t_{Cu}. Another mode, labeled d, occurred for $t_{Cu} = 5$ and 10 nm

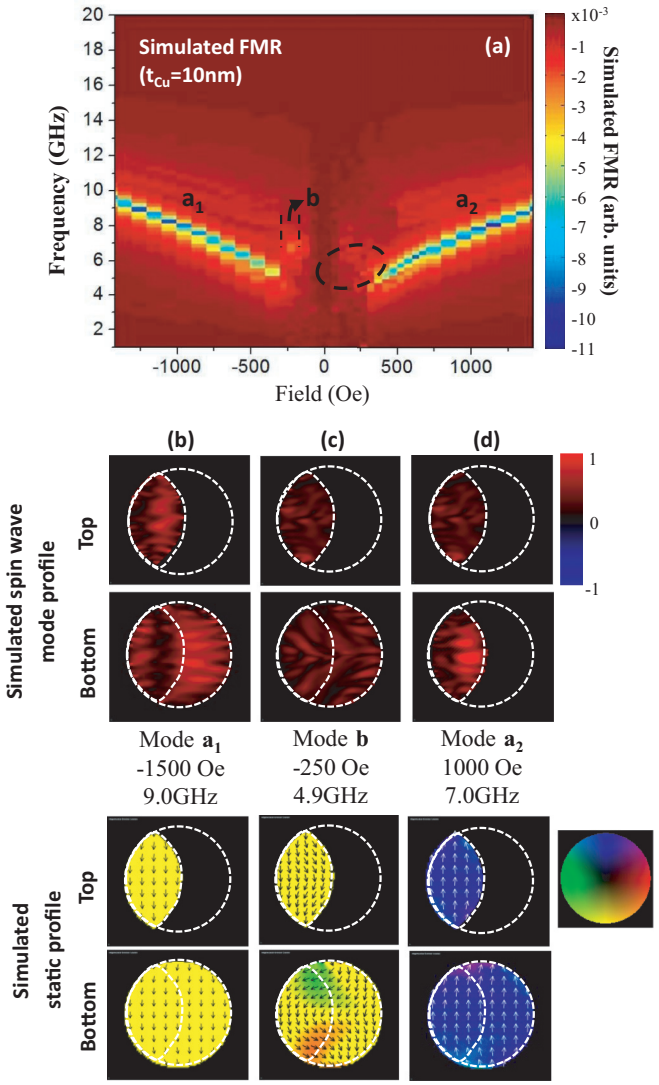

FIG. 5. (Color online) (a) Simulated FMR absorption spectra for thickness-modulated disks with $t_{Cu} = 10$ nm. Color scale bars represent relative FMR absorption intensity. (b)–(d) Simulated mode profiles (upper panels) and corresponding static spin configurations (lower panels) of top and bottom NiFe layers at various H_{app}. Color scale bar next to (d) (upper panel) represents normalized FMR absorption for (b)–(d) (upper panel). Color wheel next to (d) (lower panel) represents the component of in-plane magnetization in the disks.

between 50 and 200 Oe with $df_{res}/dH_{app} < 0$. An FMR simulation for $t_{Cu} = 10$ nm was carried out assuming the interlayer exchange constant $A_{ij} = 0$. The simulated FMR spectra in Fig. 5(a) show strong modes a_1 and a_2 and a weak mode b but did not show modes c and d (dotted lines). Figures 5(b)–5(d) show the simulated mode profiles (upper panels) and their corresponding static magnetic profiles (lower panels). Simulated mode profiles for a_1 and a_2 [Figs. 5(b) and 5(d)] differed from $t_{Cu} = 0$ nm. In the bottom NiFe disk, the region without the overlying lens-shaped layer had mode profiles similar to the $t_{Cu} = 0$ nm case. However, on the left side of the disk, the mode had complementary amplitude in the disk and in the lens, which is indicative of interlayer magnetostatic coupling. The weak mode b corresponded to the disk being in a TW configuration as in the $t_{Cu} = 0$ nm case, with the mode shape related to the nonuniform magnetization distribution in the disk [Fig. 5(c), lower panel].

Although the simulation did not predict mode c, we believe that the mode preceding the mode a_2 in the experiment corresponded to mode c: its f_{res} increased with increasing H_{app} ($df_{res}/dH_{app} > 0$), and its f_{res} dropped abruptly into mode a_2 due to vortex annihilation as the field increased. In Figs. 4(e) and 4(f), another resonance mode, labeled d, appeared ~150 and 50 Oe at $t_{Cu} = 5$ and 10 nm, respectively, preceding mode c. The characteristics of mode d are defined by the interlayer magnetostatic interaction, which occurs when t_{Cu} is large enough to exchange decouple the two layers [Figs. 4(e) and 4(f)] and promotes antiparallel orientation of the lens and disk. Mode d may then relate to the vortex propagation process from the region antiparallel to that of mode c, i.e., magnetization opposite to H_{app}. Thus, each complementary (antiparallel) domain region has its own mode excitation. In this case, it is easy to understand the origin of negative dispersion for mode d compared to mode c, which has positive dispersion. In addition, when mode d transition to mode c, the $\delta f_{d\to c}$ corresponds to the abrupt reversal in the region of magnetization opposite to H_{app}, which reduces f_{res} according to $H_y = H_{app} - H_d$. Based on analysis of mode c and d, we show that the onset of magnetostatic mode vortex propagation in each exchange-decoupled layer can be traced using FMR measurement.

IV. CONCLUSION

The dynamics of NiFe thickness-modulated disks were investigated by FMR. The different modes observed are related to the magnetization transitions in the disks, including the onset of vortex propagation and the formation of a TW configuration. Furthermore, the asymmetry introduced by the thickness modulation controlled not only the location of the vortex but also its chirality and propagation direction. The effect of interlayer magnetic interactions between the top and the bottom NiFe layers were explored by inserting a Cu spacer layer with varying thicknesses, which modified the FMR mode profile, producing complementary modes in the top and bottom NiFe layers. It is possible to distinguish the magnetostatic modes of vortex propagation in each exchange-decoupled layer using FMR measurements.

The thickness-modulated disks provide a model structure to study vortex dynamics in patterned films. This structure also offers an alternative way of controlling vortex behavior in magnetic nanostructures. These results will be useful in further development of magnetic memory, logic, and magnonic devices. For instance, using thickness modulation, an inhomogeneous internal field can be introduced in order to tailor the frequency dispersion characteristics of a magnonic crystal for a high-frequency tunable filter.[59,60] Furthermore, systematically studying the effect of interlayer coupling in this structure may lead to potential application in designing a low-power band stop filter. In magnetic memory or logic application, the accurate control of vortex chirality opens up the possibility of precisely defining the magnetic vortex handedness[2] (chirality-polarity product) for logical bit 1 or 0. The integration of such structures in magnonic crystals may

enable subnanosecond reprogramming or switching capability and offer further miniaturization in magnetic devices in the gigahertz range.[61,62]

ACKNOWLEDGMENT

The support of the Singapore-MIT Alliance is gratefully acknowledged.

*eleaao@nus.edu.sg
†caross@mit.edu

[1]K. Yamada, S. Kasai, Y. Nakatani, K. Kobayashi, H. Kohno, A. Thiaville, and T. Ono, Nat. Mater. **6**, 270 (2007).
[2]S. Bohlens, B. Kruger, A. Drews, M. Bolte, G. Meier, and D. Pfannkuche, Appl. Phys. Lett. **93**, 142508 (2008).
[3]M. P. Kostylev, A. A. Serga, T. Schneider, B. Leven, and B. Hillebrands, Appl. Phys. Lett. **87**, 153501 (2005).
[4]T. Schneider, A. A. Serga, B. Leven, B. Hillebrands, R. L. Stamps, and M. P. Kostylev, Appl. Phys. Lett. **92**, 022505 (2008).
[5]J. Ding, M. Kostylev, and A. O. Adeyeye, Appl. Phys. Lett. **100**, 073114 (2012).
[6]A. B. Ustinov and B. A. Kalinikos, Appl. Phys. Lett. **90**, 252510 (2007).
[7]Z. K. Wang, V. L. Zhang, H. S. Lim, S. C. Ng, M. H. Kuok, S. Jain, and A. O. Adeyeye, ACS Nano **4**, 643 (2010).
[8]J. P. Park, P. Eames, D. M. Engebretson, J. Berezovsky, and P. A. Crowell, Phys. Rev. B **67**, 020403 (2003).
[9]K. Perzlmaier, M. Buess, C. H. Back, V. E. Demidov, B. Hillebrands, and S. O. Demokritov, Phys. Rev. Lett. **94**, 057202 (2005).
[10]N. Kuhlmann, A. Vogel, and G. Meier, Phys. Rev. B **85**, 014410 (2012).
[11]R. Zivieri, F. Montoncello, L. Giovannini, F. Nizzoli, S. Tacchi, M. Madami, G. Gubbiotti, G. Carlotti, and A. O. Adeyeye, Phys. Rev. B **83**, 054431 (2011).
[12]C. S. Lin, H. S. Lim, C. C. Wang, A. O. Adeyeye, Z. K. Wang, S. C. Ng, and M. H. Kuok, J. Appl. Phys. **108**, 114305 (2010).
[13]M. P. Kostylev, G. Gubbiotti, J. G. Hu, G. Carlotti, T. Ono, and R. L. Stamps, Phys. Rev. B **76**, 054422 (2007).
[14]S. Tacchi, M. Madami, G. Gubbiotti, G. Carlotti, S. Goolaup, A. O. Adeyeye, N. Singh, and M. P. Kostylev, Phys. Rev. B **82**, 184408 (2010).
[15]J. Ding, M. Kostylev, and A. O. Adeyeye, Phys. Rev. Lett. **107**, 047205 (2011).
[16]J. Topp, D. Heitmann, M. P. Kostylev, and D. Grundler, Phys. Rev. Lett. **104**, 207205 (2010).
[17]G. Gubbiotti, G. Carlotti, T. Okuno, M. Grimsditch, L. Giovannini, F. Montoncello, and F. Nizzoli, Phys. Rev. B **72**, 184419 (2005).
[18]K. S. Buchanan, P. E. Roy, M. Grimsditch, F. Y. Fradin, K. Y. Guslienko, S. D. Bader, and V. Novosad, Nat. Phys. **1**, 172 (2005).
[19]I. Neudecker, K. Perzlmaier, F. Hoffmann, G. Woltersdorf, M. Buess, D. Weiss, and C. H. Back, Phys. Rev. B **73**, 134426 (2006).
[20]G. Gubbiotti, G. Carlotti, T. Okuno, T. Shinjo, F. Nizzoli, and R. Zivieri, Phys. Rev. B **68**, 184409 (2003).
[21]V. Novosad, F. Y. Fradin, P. E. Roy, K. S. Buchanan, K. Y. Guslienko, and S. D. Bader, Phys. Rev. B **72**, 024455 (2005).
[22]J. Ding, M. Kostylev, and A. O. Adeyeye, Appl. Phys. Lett. **100**, 062401 (2012).
[23]F. Giesen, J. Podbielski, T. Korn, and D. Grundler, J. Appl. Phys. **97**, 10A712 (2005).
[24]I. Neudecker, M. Kläui, K. Perzlmaier, D. Backes, L. J. Heyderman, C. A. F. Vaz, J. A. C. Bland, U. Rüdiger, and C. H. Back, Phys. Rev. Lett. **96**, 057207 (2006).
[25]T. Shinjo, T. Okuno, R. Hassdorf, K. Shigeto, and T. Ono, Science **289**, 930 (2000).
[26]R. P. Cowburn, D. K. Koltsov, A. O. Adeyeye, M. E. Welland, and D. M. Tricker, Phys. Rev. Lett. **83**, 1042 (1999).
[27]Y. S. Huang, A. O. Adeyeye, and N. Singh, J. Phys. Condens. Matter **17**, 3931 (2005).
[28]A. Lebib, S. P. Li, M. Natali, and Y. Chen, J. Appl. Phys. **89**, 3892 (2001).
[29]I. L. Prejbeanu, M. Natali, L. D. Buda, U. Ebels, A. Lebib, Y. Chen, and K. Ounadjela, J. Appl. Phys. **91**, 7343 (2002).
[30]M. Rahm, M. Schneider, J. Biberger, R. Pulwey, J. Zweck, D. Weiss, and V. Umansky, Appl. Phys. Lett. **82**, 4110 (2003).
[31]N. A. Usov and S. E. Peschany, J. Magn. Magn. Mater. **118**, L290 (1993).
[32]K. Y. Guslienko and K. L. Metlov, Phys. Rev. B **63**, 100403 (2001).
[33]K. Y. Guslienko, V. Novosad, Y. Otani, H. Shima, and K. Fukamichi, Phys. Rev. B **65**, 024414 (2001).
[34]K. Y. Guslienko, B. A. Ivanov, V. Novosad, Y. Otani, H. Shima, and K. Fukamichi, J. Appl. Phys. **91**, 8037 (2002).
[35]S. Jain, V. Novosad, F. Y. Fradin, J. E. Pearson, V. Tiberkevich, A. N. Slavin, and S. D. Bader, Nat. Comm. **3**, 1330 (2012).
[36]M. Bolte, G. Meier, B. Krüger, A. Drews, R. Eiselt, L. Bocklage, S. Bohlens, T. Tyliszczak, A. Vansteenkiste, B. Van Waeyenberge *et al.*, Phys. Rev. Lett. **100**, 176601 (2008).
[37]J. Shibata, Y. Nakatani, G. Tatara, H. Kohno, and Y. Otani, Phys. Rev. B **73**, 020403 (2006).
[38]S. Kasai, Y. Nakatani, K. Kobayashi, H. Kohno, and T. Ono, Phys. Rev. Lett. **97**, 107204 (2006).
[39]S.-K. Kim, Y.-S. Choi, K.-S. Lee, K. Y. Guslienko, and D.-E. Jeong, Appl. Phys. Lett. **91**, 082506 (2007).
[40]B. Van Waeyenberge, A. Puzic, H. Stoll, K. W. Chou, T. Tyliszczak, R. Hertel, M. Fahnle, H. Bruckl, K. Rott, G. Reiss *et al.*, Nature **444**, 461 (2006).
[41]K. Y. Guslienko, K.-S. Lee, and S.-K. Kim, Phys. Rev. Lett. **100**, 027203 (2008).
[42]Y. Liu, Z. Hou, S. Gliga, and R. Hertel, Phys. Rev. B **79**, 104435 (2009).
[43]W. Jin, H. He, Y. Chen, and Y. Liu, J. Appl. Phys. **105**, 013906 (2009).
[44]Y. Liu, S. Gliga, R. Hertel, and C. M. Schneider, Appl. Phys. Lett. **91**, 112501 (2007).
[45]M. Natali, A. Popa, U. Ebels, Y. Chen, S. Li, and M. E. Welland, J. Appl. Phys. **96**, 4334 (2004).
[46]A. Roman, U. Michal, and O. Yoshichika, J. Phys. Conf. **200**, 042002 (2010).
[47]M. Natali, I. L. Prejbeanu, A. Lebib, L. D. Buda, K. Ounadjela, and Y. Chen, Phys. Rev. Lett. **88**, 157203 (2002).
[48]M. Schneider, H. Hoffmann, and J. Zweck, Appl. Phys. Lett. **79**, 3113 (2001).

[49]T. Kimura, Y. Otani, H. Masaki, T. Ishida, R. Antos, and J. Shibata, Appl. Phys. Lett. **90**, 132501 (2007).
[50]Y. Nozaki, K. Tateishi, S.-I. Taharazako, S. Yoshimura, and K. Matsuyama, J. Appl. Phys. **105**, 013911 (2009).
[51]Y.-Y. Au and S. Ingvarsson, J. Appl. Phys. **106**, 083906 (2009).
[52]G. Gubbiotti, M. Kostylev, N. Sergeeva, M. Conti, G. Carlotti, T. Ono, A. N. Slavin, and A. Stashkevich, Phys. Rev. B **70**, 224422 (2004).
[53]Y. Nozaki, K. Tateishi, S. Taharazako, S. Yoshimura, and K. Matsuyama, Appl. Phys. Lett. **92**, 161903 (2008).
[54]A. O. Adeyeye and N. Singh, J. Phys. D **41**, 153001 (2008).
[55]G. Shimon, A. O. Adeyeye, and C. A. Ross, Appl. Phys. Lett. **101**, 083112 (2012).
[56]J. M. D. Coey, *Magnetism and Magnetic Materials* (Cambridge University Press, New York, 2010).
[57]M. R. Scheinfein and E. A. Price, LLG Micromagnetics Simulator, software for micromagnetic simulations.
[58]C. Kittel, Phys. Rev. **73**, 155 (1948).
[59]G. Gubbiotti, S. Tacchi, M. Madami, G. Carlotti, A. O. Adeyeye, and M. Kostylev, J. Phys. D **43**, 264003 (2010).
[60]N. N. Phuoc, F. Xu, and C. K. Ong, Appl. Phys. Lett. **94**, 092505 (2009).
[61]S. Pal, B. Rana, O. Hellwig, T. Thomson, and A. Barman, Appl. Phys. Lett. **98**, 082501 (2011).
[62]Y. Nozaki, N. Narita, T. Tanaka, and K. Matsuyama, Appl. Phys. Lett. **95**, 082505 (2009).